Precipitation of metal sulphides using gaseous hydrogen sulphide

Tarazi, Mousa Al-; Heesink, A. Bert M.; Versteeg, Geert F.

Published in:
Chemical Engineering Science

DOI:
10.1016/j.ces.2003.11.006

Publication date:
2004

ELSEVIER

Chemical Engineering Science 59 (2004) 567–579

Chemical Engineering Science

www.elsevier.com/locate/ces

Precipitation of metal sulphides using gaseous hydrogen sulphide: mathematical modelling

Mousa Al-Tarazi*, A. Bert M. Heesink, Geert F. Versteeg

Faculty of Science and Technology, University of Twente, P.O. Box 217, Enschede, The Netherlands

Received 1 July 2003; received in revised form 23 September 2003; accepted 4 November 2003

Abstract

A mathematical model has been developed that describes the precipitation of metal sulffides in an aqueous solution containing two different heavy metal ions. The solution is assumed to consist of a well-mixed bulk and a boundary layer that is contacted with hydrogen sulphide gas. The model makes use of Higbie's penetration model to calculate the transfer of gaseous hydrogen sulphide to this boundary layer. The conditions that have been used in the simulations resemble those of industrial wastewater from a zinc factory. The model predicts the rate of H_2S absorption, the size distribution of the metal sulphide crystals and the selectivity of precipitation. Higher precipitation rates are predicted at higher pH values and higher H_2S concentrations. In all cases considered, the rate of precipitation is fully controlled by mass transfer of H_2S, higher H_2S concentrations and higher specific surface areas yielding higher precipitation rates. The size of the obtained crystals is predicted to increase with H_2S concentration, but to decrease with specific surface area and liquid side mass transfer. These results illustrate the importance of reactor layout and operating conditions on the process of gas–liquid precipitation.

Keywords: Absorption; Mass transfer; Modelling; Multiphase reactor; Precipitation; Gas–liquid

1. Introduction

Crystallization involves the transformation of an amorphous solid, a liquid or a gas into the crystalline state (Mersmann, 1995). As with any chemical process, a certain driving force is needed to accomplish this task; in crystallization this driving force is delivered by supersaturation. Supersaturation can be achieved by cooling the solution, evaporating the solvent, adding an inert substance that reduces the solubility (drowning out) or by reaction. Precipitation, or reactive crystallization, involves the reaction of two or more reactants to form a sparingly soluble product, which then becomes supersaturated and, as a result, crystallizes.

Precipitation of solids promoted by gas–liquid reactions takes place in many industrial processes (Wachi and Jones, 1991). Despite the importance of this principle (in this paper further referred to as "gas–liquid precipitation"), no extensive studies have been dedicated to it until recently. The size distribution of the solid particles is fully determined by precipitation conditions, which may vary quite significantly from the gas–liquid interface to the liquid bulk. This size distribution is of great importance for separation and downstream processing of the particles. A good understanding of the relevant phenomena is therefore of utmost interest.

Gas–liquid precipitation is applied for the synthesis of many chemicals such as ammonium phosphate, ammonium sulphate, barium carbonate, calcium carbonate, calcium fluoride, gypsum (calcium sulphate), goethite, sodium bicarbonate, strontium carbonate and terephthalic acid (Wachi and Jones, 1995). In addition, gas–liquid precipitation can be applied in gas cleaning, heavy metal removal and in biotechnology (Paques, www.paques.nl). This paper deals with the simultaneous precipitation of two heavy metal ions by gaseous H_2S and the modelling thereof.

The process of gas–liquid precipitation generally involves mass transfer, chemical reaction, supersaturation, nucleation, molecular growth, agglomeration, disruption and ripening. During the so-called induction period mass

* Corresponding author. Tel.: +31-53-489-4337; fax: +31-53-489-4774.
E-mail address: tarazi@ct.utwente.nl (M. Al-Tarazi).
URL: http://www.utwente.nl

0009-2509/$ - see front matter © 2003 Elsevier Ltd. All rights reserved.
doi:10.1016/j.ces.2003.11.006

transfer and chemical reaction cause the generation of supersaturation. Nucleation and subsequent crystal growth then follow at a rate that depends on the delivered level of supersaturation. The size of solids formed upon nucleation will increase by molecular or ionic growth at the crystal surface as well as by agglomeration. Small crystals may also dissolve while the resulting solute is transported to the larger crystals, which are thermodynamically more stable and will grow (Ostwald ripening). All mentioned phenomena occur simultaneously and are inter-related, making gas–liquid precipitation a rather complex process. By precisely describing each phenomenon and combining the obtained submodels in a comprehensive overall model, a tool is obtained that can be used to predict the particle size distribution of the obtained particles as a function of reactor layout and operating conditions.

The layout of the gas–liquid contactor is of substantial importance for product quality as well as for production efficiency. Compare, for example, a spray tower with a bubble column: mass transfer and mixing phenomena are completely different in these contactors and the size distributions of the produced particles in both contactors will most probably differ. Each stage of particle formation is affected by the way of gas–liquid contacting. Gas–liquid mass transfer phenomena determine the level of solute supersaturation and its spatial distribution in the liquid phase. Agglomeration and subsequent ageing processes are likely to be affected by flow dynamics, motion of the suspended solids and by fluid shear stress distribution as well.

Thus during precipitation of dissolved species with gaseous compounds, mass transfer often controls overall precipitation behaviour and product characteristics (Versteeg et al., 1989). Nevertheless, its effect has not yet been studied extensively, even though small differences in concentrations at micro-level may highly influence the size of the obtained crystals due to the high sensitivity of nucleation kinetics and crystal growth towards the level of supersaturation.

2. Previous work

Wachi and Jones (1991) modelled the gas–liquid precipitation of calcium carbonate using gaseous CO_2. Gas–liquid mass transfer, chemical reaction and crystallization were analysed making use of the film theory to describe gas–liquid mass transfer coupled with chemical reaction. Mass and population balances were used to calculate the obtained particle size distribution. They solved the resulting equations for a stirred cell reactor, operated in semi-batch mode. They calculated that the spatial distribution of supersaturation due to the mass transfer resistance has an effect on the resulting crystal size distribution: according to model prediction larger particles are formed under conditions of fast mass transfer, while small particles of uniform size are produced when mass transfer is slow.

Narayan S. Tavare (1991) reviewed the techniques employed for the evaluation of experimental data from batch crystallizers. They presented a number of useful general techniques to extract crystallization kinetics and to assess crystallizer performance.

Jones et al. (1992) studied the effect of liquid mixing on primary crystal size during the precipitation of calcium carbonate in stirred cell. They used the film model to describe gas–liquid mass transfer coupled with chemical reaction and a dynamic population balance to describe crystal growth. Experimentally, they found that small crystals of approx. 1 μm are formed in the vicinity of the gas–liquid interface during the early stages of batch precipitation. The primary crystals were found to grow reaching a diameter of approximately 6 μm in the bulk. This mean crystal size was found to increase with increasing agitation rate that is consistent with model predictions.

Wachi and Jones (1992) studied the influence of agglomeration on the gas–liquid precipitation of calcium carbonate. They described the effects of agglomeration using two extra terms in the population balance (birth and death). Their model predicts the evolution of particle size distribution in time. They found that the formation of agglomerated precipitates can be modelled in terms of overall particle size and the number of primary crystals within a particle.

Wachi and Jones (1995) reviewed gas–liquid precipitation with particular focus on how to control the physical form of the product. They also examined the secondary processes of particle agglomeration and particle disruption and the effects of reactor fluid dynamics.

Hostomsky and Jones (1995) modelled the precipitation of calcium carbonate crystals in a semi-batch stirred cell using Higbie's penetration model to describe gas–liquid mass transfer. They studied the effect of mass transfer on the rate of precipitation using thermodynamic and kinetic data from literature. They found that the nucleation rate in the region close to the gas–liquid interface will increase with decreasing mass transfer rates. However, at very low mass transfer rates (i.e. long contact times), nucleation rates become inhibited by the depletion of Ca^{2+} ions. They also found that at low mass transfer rates, nucleation predominantly proceeds in the interfacial region rather than in the bulk solution. They predicted that the nucleation rate, particle number density and mean particle size show a maximum at a position away from the gas–liquid interface.

Al-Rahed and Jones (1999) performed a CFD analysis to predict the effect of mixing during batch-wise gas–liquid precipitation. They developed a 2D flow simulation model and compared their CFD-based predictions with the results of the applied film and penetration models for the calcium carbonate system. They found out that CFD-based predictions reveal crystal size distributions in between those predicted by the film model and the penetration model, thereby highlighting the role of hydrodynamics in the precipitation process.

3. Present model

In this work, a more comprehensive mathematical model has been developed that describes the simultaneous precipitation of two different heavy metal ions (Cu^{2+} and Zn^{2+} are taken as example) in an aqueous solution that is continuously contacted with hydrogen sulphide gas in a stirred cell (Fig. 1). This model is able to predict the effects of operating conditions and reactor layout on the rate of precipitation and the size distribution of the produced particles. It does so for two different precipitates and thus predicts selectivity. The model makes use of Higbie's penetration model to calculate the transfer of gaseous hydrogen sulphide to the aqueous liquid. Besides the liquid side mass transfer resistance also the gas side resistance is considered in the model. Mass balances for all species and the electroneutrality demand are used to calculate concentration profiles. The required equilibrium and kinetic data were taken from literature. The model includes nucleation and crystal growth in the film layer as well as in the bulk. Both gas and liquid bulk are assumed to be ideally mixed and the H_2S concentration in the gas bulk is assumed not to change in time. Besides the two heavy metal ions, sulphate ions are assumed to be present in the liquid. In this way the composition of a typical wastewater stream as frequently encountered in metal production plants is resembled.

The chemistry of the mixed ions system can be described by the following equations:

$$H_2S_{(g)} \leftrightarrow H_2S_{(L)}, \tag{A}$$

$$H_2S_{(L)} \overset{k_1,\frac{k_1}{k_{eq1}}}{\longleftrightarrow} HS^- + H^+, \tag{B}$$

$$HS^- \overset{k_2,\frac{k_2}{k_{eq2}}}{\longleftrightarrow} S^{2-} + H^+, \tag{C}$$

$$Me_1^{2+} + S^{2-} \xrightarrow{k_3} Me_1S, \tag{D}$$

$$Me_2^{2+} + S^{2-} \xrightarrow{k_4} Me_2S, \tag{E}$$

$$H^+ + OH^- \overset{k_5,k_5k_w}{\longleftrightarrow} H_2O, \tag{F}$$

$$HSO_4^- \overset{k_6,\frac{k_6}{k_s}}{\longleftrightarrow} SO_4^{2-} + H^+. \tag{G}$$

"Reaction" (A) occurs only at the gas–liquid interface. The concentration of dissolved H_2S at the gas–liquid interface is calculated by an iterative procedure involving the gas side mass transfer rate and Henry's law. The reversible reactions (B), (C), (F) and (G) are very fast and are assumed to be at equilibrium. However, for numerical reasons kinetic constants are used (having very high values; see Table 1). The consumption rates are calculated according

$$r_{H_2S} = k_1 c_{H_2S} - \frac{k_1}{k_{eq_1}} c_{HS^-} c_{H^+}, \tag{1}$$

$$r_{HS^-} = k_2 c_{HS^-} - \frac{k_2}{k_{eq_2}} c_{S^{2-}} c_{H^+} - k_1 c_{H_2S_{(L)}} + \frac{k_1}{k_{eq_1}} c_{HS^-} c_{H^+}, \tag{2}$$

$$r_{S^{2-}} = -k_2 c_{HS^-} + \frac{k_2}{k_{eq_2}} c_{S^{2-}} c_{H^+} + r_{Me_1S} + r_{Me_2S}, \tag{3}$$

$$r_{Me_1^{2+}} = -r_{Me_1S}, \tag{4}$$

$$r_{Me_2^{2+}} = -r_{Me_2S}, \tag{5}$$

$$r_{H^+} = -k_1 c_{H_2S_{LL)}} + \frac{k_1}{k_{eq_1}} c_{HS^-} c_{H^+} - k_2 c_{HS^-} + \frac{k_2}{k_{eq_2}} c_{S^{2-}} c_{H^+} + k_5 c_{H^+} c_{OH^-} - k_6 c_{HSO_4^-} + \frac{k_6}{k_{eq_3}} c_{SO_4^{2-}} c_{H^+} - k_5 k_w, \tag{6}$$

$$r_{OH^-} = k_5 c_{H^+} c_{OH^-} - k_5 k_w, \tag{7}$$

$$r_{HSO_4^-} = k_6 c_{HSO_4^-} - \frac{k_6}{k_{eq_3}} c_{H^+} c_{SO_4^{2-}}, \tag{8}$$

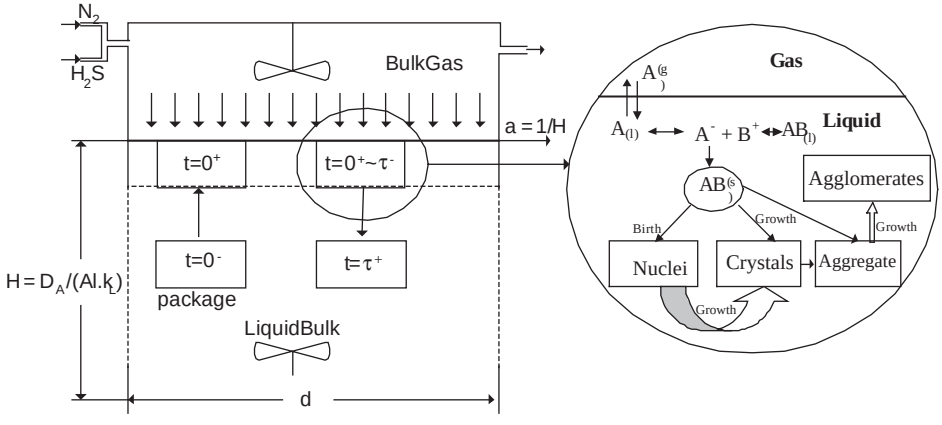

Fig. 1. Schematic diagram of the gas–liquid contactor applied in the model. Formation of aggregates and agglomerates is not included in this present model.

Table 1
List of numerical values for the constants used in the model (1 = Cu, 2 = Zn)

Parameters	Value		Source
k_{sp_1}	6.3×10^{-30}	(mol^2/m^6)	[16]
k_{sp2}	1.6×10^{-18}	(mol^2/m^6)	[16]
ρ_1	41650.0	(mol/m^3)	[16]
ρ_2	45420.0	(mol/m^3)	[16]
L_{01}	5.6655×10^{-7}	(m)	[1]
L_{02}	5.392×10^{-7}	(m)	[1]
g_1	1.3	(dimensionless)	[17]
g_2	1.5	(dimensionless)	[17]
n_1	3.0	(dimensionless)	[17]
n_2	4.2	(dimensionless)	[17]
k_{n_1}	1.1×10^{-23}	(m/s)	[17]
k_{n_2}	1.3×10^{-13}	(dimensionless)	[17]
k_{g_1}	2.06×10^{-20}	(m/s)	[17]
k_{g_2}	1.96×10^{-14}	(m/s)	[17]
α	$\pi/6$	(dimensionless)	For spherical particles
β	π	(dimensionless)	For spherical particles
$D_{H_2S(L)}$	1.92×10^{-9}	(m^2/s)	[18]
$D_{H_2S(g)}$	2.366×10^{-4}	(m^2/s)	[18]
D_{HS^-}	1.731×10^{-9}	(m^2/s)	[18]
$D_{S^{2-}}$	1.03×10^{-9}	(m^2/s)	[19]
$D_{Me_1^{2+}}$	0.703×10^{-9}	(m^2/s)	[18]
$D_{Me_2^{2+}}$	0.714×10^{-9}	(m^2/s)	[17]
D_{H^+}	9.311×10^{-9}	(m^2/s)	[18]
D_{OH^-}	5.273×10^{-9}	(m^2/s)	[18]
$D_{HSO_4^-}$	1.331×10^{-9}	(m^2/s)	[18]
$D_{SO_4^{2-}}$	1.065×10^{-9}	(m^2/s)	[18]
$m(c_L^i/c_g^i)$	3.1773	(dimensionless)	[18]
k_1	1×105	(1/s)	Assumed
k_2	3×10^{11}	(m^3/mol s)	Assumed
k_3	5×10^{12}	(m^3/mol s)	Assumed
k_4	3×10^{12}	(m^3/mol s)	Assumed
k_5	2.2×10^{15}	(m^3/mol s)	Assumed
k_6	1×10^2	(1/s)	Assumed
$k_{m,g}$	1.0×10^{-2}	(m/s)	Assumed
k_{eq} (HSO_4^-/SO_4^{2-})	10.233	(mol/m^3)	[18]
k_{eq} (H_2S/HS^-)	1.07152×10^{-4}	(mol/m^3)	[18]
k_{eq} (HS^-/S^{2-})	1.259×10^{-10}	(mol/m^3)	[18]
k_w	1×10^{-8}	(mol^2/m^6)	[18]

$$r_{SO_4^{2-}} = -k_6 c_{HSO_4^-} + \frac{k_6}{k_{eq_3}} c_{H^+} c_{SO_4^{2-}}, \tag{9}$$

$$-r_{Me_1S} = G_1' + B_1' - \sqrt{k_{sp_1}}, \tag{10}$$

$$-r_{Me_2S} = G_2' + B_2' - \sqrt{k_{sp_2}}, \tag{11}$$

According to Higbie's penetration model (Higbie, 1935), stagnant packages of solution arise from the bulk, move to the gas–liquid interface, remain there for a certain period of time (contact time τ) and are then swept back to the bulk. The concentration profiles of all individual species in the liquid package can be calculated as a function of time using the following equations (mass balances):

$$\frac{\partial c_{H_2S_{(L)}}}{\partial t} = D_{H_2S_{(L)}} \frac{\partial^2 c_{H_2S_{(L)}}}{\partial x^2} - r_{H_2S}, \tag{12}$$

$$\frac{\partial c_{HS^-}}{\partial t} = D_{HS^-} \frac{\partial^2 c_{HS^-}}{\partial x^2} - z_{HS^-} D_{HS^-} \frac{F}{RT} \frac{\partial(\phi c_{HS^-})}{\partial x} - r_{HS^-}, \tag{13}$$

$$\frac{\partial c_{S^{2-}}}{\partial t} = D_{S^{2-}} \frac{\partial^2 c_{S^{2-}}}{\partial x^2} - z_{S^{2-}} D_{S^{2-}} \frac{F}{RT} \frac{\partial(\phi c_{S^{2-}})}{\partial x} - r_{S^{2-}}, \tag{14}$$

$$\frac{\partial c_{Me_1^{2+}}}{\partial t} = D_{Me_1^{2+}} \frac{\partial^2 c_{Me_1^{2+}}}{\partial x^2} - z_{Me_1^{2+}} D_{Me_1^{2+}} \frac{F}{RT} \frac{\partial(\phi c_{Me_1^{2+}})}{\partial x} - r_{Me_1^{2+}}, \tag{15}$$

$$\frac{\partial c_{Me_2^{2+}}}{\partial t} = D_{Me_2^{2+}} \frac{\partial^2 c_{Me_2^{2+}}}{\partial x^2} - z_{Me_2^{2+}} D_{Me_2^{2+}} \frac{F}{RT} \frac{\partial(\phi c_{Me_2^{2+}})}{\partial x} - r_{Me_2^{2+}}, \tag{16}$$

$$\frac{\partial c_{H^+}}{\partial t} = D_{H^+} \frac{\partial^2 c_{H^+}}{\partial x^2} - z_{H^+} D_{H^+} \frac{F}{RT} \frac{\partial(\phi c_{H^+})}{\partial x} - r_{H^+}, \tag{17}$$

$$\frac{\partial c_{OH^-}}{\partial t} = D_{OH^-} \frac{\partial^2 c_{OH^-}}{\partial x^2} - z_{OH^-} D_{OH^-} \frac{F}{RT} \frac{\partial(\phi c_{OH^-})}{\partial x} - r_{OH^-}, \tag{18}$$

$$\frac{\partial c_{HSO_4^-}}{\partial t} = D_{HSO_4^-} \frac{\partial^2 c_{HSO_4^-}}{\partial x^2} - z_{HSO_4^-} D_{HSO_4^-} \frac{F}{RT} \frac{\partial(\phi c_{HSO_4^-})}{\partial x} - r_{HSO_4^-}, \tag{19}$$

$$\frac{\partial c_{SO_4^{2-}}}{\partial t} = D_{SO_4^{2-}} \frac{\partial^2 c_{SO_4^{2-}}}{\partial x^2} - z_{SO_4^{2-}} D_{SO_4^{2-}} \frac{F}{RT} \frac{\partial(\phi c_{SO_4^{2-}})}{\partial x} - r_{SO_4^{2-}}. \tag{20}$$

The mass balances of Me_1S and Me_2S are not needed since the rate of crystal growth and nucleation are expressed as separate functions of supersaturation and population balances are used (see below).

The electrostatic potential gradient (ϕ) can be calculated by the use of the Nernst–Einstein (Newman, 1973) equation assuming dynamic electroneutrality

$$\phi(x,t) = \frac{RT}{F} \frac{\sum_{i=1}^{NC} z_i D_i \partial c_i/\partial x}{\sum_{i=1}^{NC} z_i^2 D_i c_i}. \tag{21}$$

Assuming no agglomeration or attrition (death and secondary nucleation), the crystal size distribution follows from the population balance proposed by Randolph and Larson (1988)

$$\frac{\partial n_1}{\partial t} + G_1 \left(\frac{\partial n_1}{\partial L} \right) = D_{p_1} \frac{\partial^2 n_1}{\partial x^2}, \tag{22}$$

$$\frac{\partial n_2}{\partial t} + G_2\left(\frac{\partial n_2}{\partial L}\right) = D_{p_2}\frac{\partial^2 n_2}{\partial x^2}. \tag{23}$$

Diffusion of particles is mainly due to random motion of these particles. Incorporating of this term is important since the packages are assumed to be stagnant (Higbie's penetration model). Migration of particles within a package will influence the growth rate as well as the mean particle size distribution within that package. For sufficiently small particles, the diffusivity of the crystals within the liquid film may be described by the Stokes–Einstein equation (Sutherland, 1905)

$$D_p = \frac{k_b T}{6\pi\eta r}. \tag{24}$$

The rate of nucleation (J_n), the linear growth rate (G) and the molar growth rate (G) are given by

$$G = k_g\left[\frac{\sqrt{c_{Me^{2+}}c_{S^{2-}}}}{c^*_{MeS}} - 1\right]^g, \tag{25}$$

$$J_n = k_n\left[\frac{\sqrt{c_{Me^{2+}}c_{S^{2-}}}}{c^*_{MeS}} - 1\right]^n, \tag{26}$$

$$B' = \alpha\rho J_n L_o^3, \tag{27}$$

$$G' = \sum_{i=1}^{\infty}\{\beta\rho n(z, L_i^2)GL_i^2(L_i - L_{i-1})\}, \tag{28}$$

$$c^*_{MeS} = \sqrt{k_{sp}}. \tag{29}$$

The initial and boundary conditions for the above equations are

$$c_i(t=0) = c_i^{bulk}, \tag{30}$$

$$n(x, L, t=0) = n(L)_{bulk}. \tag{31}$$

To derive the appropriate boundary conditions near the gas–liquid interface, mass balances over a control volume of thickness Δx should be used for all species

$$\frac{\partial}{\partial t}\int_0^{\Delta x} c_{H_2S}\,dx = J_{H_2S} + D_{HS^-}\frac{\partial c_{H_2S}}{\partial x} - \int_0^{\Delta x} r_{H_2S}\,dx, \tag{32a}$$

$$\frac{\partial}{\partial t}\int_0^{\Delta x} c_{HS^-}\,dx = D_{HS^-}\frac{\partial c_{HS^-}}{\partial x} - z_{HS^-}D_{HS^-}\frac{F}{RT}\phi c_{HS^-} - \int_0^{\Delta x} r_{HS^-}\,dx, \tag{32b}$$

$$\frac{\partial}{\partial t}\int_0^{\Delta x} c_{S^{2-}}\,dx = D_{S^{2-}}\frac{\partial c_{S^{2-}}}{\partial x} - z_{S^{2-}}D_{S^{2-}}\frac{F}{RT}\phi c_{S^{2-}} - \int_0^{\Delta x} r_{S^{2-}}\,dx, \tag{32c}$$

$$\frac{\partial}{\partial t}\int_0^{\Delta x} c_{H^+}\,dx = D_{H^+}\frac{\partial c_{H^+}}{\partial x} - z_{H^+}D_{H^+}\frac{F}{RT}\phi c_{H^+} - \int_0^{\Delta x} r_{H^+}\,dx, \tag{32d}$$

$$\frac{\partial}{\partial t}\int_0^{\Delta x} c_{HO^-}\,dx = D_{HO^-}\frac{\partial c_{HO^-}}{\partial x} - z_{HO^-}D_{HO^-}\frac{F}{RT}\phi c_{HO^-} - \int_0^{\Delta x} r_{HO^-}\,dx, \tag{32e}$$

$$\frac{\partial}{\partial t}\int_0^{\Delta x} c_{HSO_4^-}\,dx = D_{HSO_4^-}\frac{\partial c_{HSO_4^-}}{\partial x} - z_{HSO_4^-}D_{HSO_4^-}\frac{F}{RT}\phi c_{HSO_4^-} - \int_0^{\Delta x} r_{HSO_4^-}\,dx, \tag{32f}$$

$$\frac{\partial}{\partial t}\int_0^{\Delta x} c_{SO_4^{2-}}\,dx = D_{SO_4^{2-}}\frac{\partial c_{SO_4^{2-}}}{\partial x} - z_{SO_4^{2-}}D_{SO_4^{2-}}\frac{F}{RT}\phi c_{SO_4^{2-}} - \int_0^{\Delta x} r_{SO_4^{2-}}\,dx, \tag{32g}$$

$$\frac{\partial}{\partial t}\int_0^{\Delta x} c_{Me_1^{2+}}\,dx = D_{Me_1^{2+}}\frac{\partial c_{Me_1^{2+}}}{\partial x} - z_{Me_1^{2+}}D_{Me_1^{2+}}\frac{F}{RT}\phi c_{Me_1^{2+}} - \int_0^{\Delta x} r_{Me_1^{2+}}\,dx, \tag{32h}$$

$$\frac{\partial}{\partial t}\int_0^{\Delta x} c_{Me_2^{2+}}\,dx = D_{Me_2^{2+}}\frac{\partial c_{Me_2^{2+}}}{\partial x} - z_{Me_2^{2+}}D_{Me_2^{2+}}\frac{F}{RT}\phi c_{Me_2^{2+}} - \int_0^{\Delta x} r_{Me_2^{2+}}\,dx. \tag{32i}$$

For an instantaneous reaction the reaction rate becomes infinite and therefore integration is not possible. In such cases elimination of the rate terms in the above equations can be achieved by adding or subtracting those mass balances that are linked by the accumulation terms. By doing so the accumulation terms vanish, while the time derivatives of all concentrations are assumed to remain bounded. Accordingly, the following boundary conditions are obtained:

$$J_{H_2S} + \begin{bmatrix} D_{HS^-}\dfrac{\partial c_{H_2S}}{\partial x} + D_{HS^-}\dfrac{\partial c_{HS^-}}{\partial x} - z_{HS^-}D_{HS^-}\dfrac{F}{RT}\phi c_{HS^-} \\ +D_{S^{2-}}\dfrac{\partial c_{S^{2-}}}{\partial x} - z_{S^{2-}}D_{S^{2-}}\dfrac{F}{RT}\phi c_{S^{2-}} - D_{Me_1^{2+}}\dfrac{\partial c_{Me_1^{2+}}}{\partial x} \\ +z_{Me_1^{2+}}D_{Me_1^{2+}}\dfrac{F}{RT}\phi c_{Me_1^{2+}} - D_{Me_2^{2+}}\dfrac{\partial c_{Me_2^{2+}}}{\partial x} \\ +z_{Me_2^{2+}}D_{Me_2^{2+}}\dfrac{F}{RT}\phi c_{Me_2^{2+}} \end{bmatrix} = 0, \tag{33a}$$

$$2J_{H_2S} + \left[\begin{array}{l} D_{H^+}\dfrac{\partial c_{H^+}}{\partial x} - z_{H^+}D_{H^+}\dfrac{F}{RT}\phi c_{H^+} - D_{HO^-}\dfrac{\partial c_{HO^-}}{\partial x} \\ +z_{HO^-}D_{HO^-}\dfrac{F}{RT}\phi c_{HO^-} + D_{HSO_4^-}\dfrac{\partial c_{HSO_4^-}}{\partial x} \\ -z_{HSO_4^-}D_{HSO_4^-}\dfrac{F}{RT}\phi c_{HSO_4^-} + D_{HS^-}\dfrac{\partial c_{HS^-}}{\partial x} \\ -z_{HS^-}D_{HS^-}\dfrac{F}{RT}\phi c_{HS^-} + 2D_{HS^-}\dfrac{\partial c_{H_2S}}{\partial x} \end{array}\right]_{x=0} = 0, \tag{33b}$$

$$\left[\begin{array}{l} D_{HSO_4^-}\dfrac{\partial c_{HSO_4^-}}{\partial x} - z_{HSO_4^-}D_{HSO_4^-}\dfrac{F}{RT}\phi c_{HSO_4^-} \\ +D_{SO_4^{2-}}\dfrac{\partial c_{SO_4^{2-}}}{\partial x} - z_{SO_4^{2-}}D_{SO_4^{2-}}\dfrac{F}{RT}\phi c_{SO_4^{2-}} \end{array}\right]_{x=0} = 0, \tag{33c}$$

This elimination process gives three independent equations (33(a)–(c)). To achieve the complete boundary conditions the following six equations expressing the chemical equilibria are accomplished are also needed:

$$k_{eq_1}c_{H_2S} - c_{HS^-}c_{H^+} = 0, \tag{33d}$$

$$k_{eq_2}c_{HS^-} - c_{H^+}c_{S^{2-}} = 0, \tag{33e}$$

$$k_{sp_1} - c_{S^{2-}}c_{Me_1^{2+}} = 0, \tag{33f}$$

$$k_{sp_2} - c_{S^{2-}}c_{Me_2^{2+}} = 0, \tag{33g}$$

$$k_w - c_{H^+}c_{OH^-} = 0, \tag{33h}$$

$$k_{eq_3}c_{HSO_4^-} - c_{H^+}c_{SO_4^{2-}} = 0. \tag{33i}$$

However, the use of far more simplified boundary conditions will give similar results (Versteeg et al., 1989). Therefore, in order to reduce the calculation time and to improve numerical stability, commonly the following simplified boundary conditions were used:

$$-D_{H_2S}\left.\frac{\partial c_{H_2S}}{\partial x}\right|_{x=0} = k_{m,g}\left(c^{bulk}_{H_2S_{(g)}} - \frac{c^{i}_{H_2S_{(L)}}}{m}\right)$$

for H_2S (34)

and for the other components

$$z_iD_i\frac{F}{RT}(\phi c_i)\Big|_{x=0} - D_i\left.\frac{\partial c_i(t)}{\partial x}\right|_{x=0} = 0$$

for ionic components, (35)

$$\left.\frac{\partial c_i(t)}{\partial x}\right|_{x=0} = 0 \quad \text{for neutral non-volatile components,} \tag{36}$$

$$c_i(t)_{x=z_0} = c_i^{bulk}(t). \tag{37}$$

The thickness of the package is calculated using the film model for the most diffusive species, i.e. hydrogen ions. For safety reasons this thickness is multiplied by two to make sure that the condition of "infinite" package thickness is obliged

$$z_0 = 2\frac{D_{H^+}}{k_{m,L}}, \tag{38}$$

$$\left(\frac{\partial n}{\partial x}\right)_{x=0} = 0, \tag{39}$$

$$\frac{dn(x,L_0,t)}{dt} = J_nG$$

where L_0 is the critical size of a nucleus. (40)

The equations describing the concentration profiles in the package are coupled with the equations that describe the time-dependent concentrations and particle size distribution in the well-mixed bulk by means of the changing boundary conditions and initial conditions

$$\frac{\partial c_i^{bulk}}{\partial t} = -r_i, \tag{41}$$

$$\frac{\partial n_k}{\partial t} + G_k\left(\frac{\partial n_k}{\partial L}\right) = 0 \quad \text{where } k \text{ can be } Me_1 \text{ or } Me_2. \tag{42}$$

The initial concentrations of all species in a package and liquid bulk as well as the initial particle size distribution are updated after each penetration time by mixing the concentrations and particle size distribution in the bulk with the average concentrations and particle size distribution in the returning packages in a weighed manner (Fig. 2 illustrates the applied algorithm)

$$c_i^{bulk}(t=\tau) = \frac{Al-1}{Al}c_i^{bulk}(t=\tau^-) + \frac{1}{Al}\sum_{k=0}^{n}c_i^{package}(x_k,\tau^-)(x_{k+1}-x_k), \tag{43}$$

where Al is the Hinterland ratio (volume of packages/total volume of liquid).

In this manner, it is ensured that the calculated concentrations and particle size distributions are the average of both bulk and film layer.

The time derivative and the second partial derivatives of the above model equations are discretized using the proposed scheme by Baker and Oliphant (1960). The convection term (electroneutrality term) is discretized using the first-order upwind scheme. In this model the boundary conditions at the liquid bulk side of the package are updated every time step by recalculation of the bulk concentrations while making use of Eqs. (41) and (42).

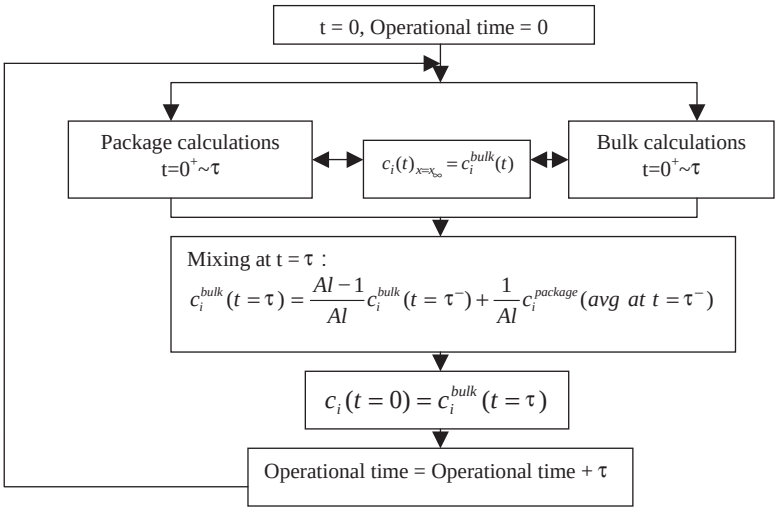

Fig. 2. Algorithm for calculation of bulk concentrations; same routine is used for particle size distribution.

The model has been applied to simulate the simultaneous precipitation of copper and zinc ions with H_2S. Most data necessary to solve the model have been taken from literature (see Table 1).

4. Results and discussion

The model was used to predict the effects of mass transfer coefficient, specific gas–liquid area, pH, metal concentration and H_2S gas concentration on the simultaneous precipitation of copper and zinc. A semi-batch reactor with a liquid volume of 0.001 m^3 was simulated (see Fig. 1). The specific gas–liquid surface area of this reactor amounts to 0.785 m^2/m^3 (when operated as a stirred cell). The standard simulation involves a temperature of 298 K, a pressure of 1 bar, a gas side mass transfer coefficient ($k_{m,g}$) of 1×10^{-2} m/s (in case of gas mixtures), a H_2S concentration of 10 vol%, a liquid side mass transfer coefficient ($k_{m,L}$) of 5×10^{-4} m/s, an initial Cu^{2+} concentration of 6 mol/m^3, an initial Zn^{2+} concentration of 6 mol/m^3 and an initial pH of 5 (before adding any $CuSO_4$ or $ZnSO_4$).

The calculated concentration profile of H_2S inside a fresh package (not containing any precipitate yet) as a function of time is shown in Fig. 3a for the standard case defined above. At the beginning the concentration profile is very steep due to the precipitation reaction near the interface and due to the fact that the package initially is completely free of H_2S. When time increases, the H_2S concentration near the interface increases while the metal concentration near the surface decreases resulting in lower reaction rates and consequently lower H_2S fluxes. The concentration of S^{2-} in the package is 2 orders of magnitude less than the values calculated for H_2S absorption in clear water due to the consumption of S^{2-} in the reaction with Cu^{2+} and Zn^{2+} (see also Fig. 3b). Typical concentration profiles of H_2S, HS^-, S^{2-}, Cu^{2+} and Zn^{2+} at the end of the penetration time are shown in Fig. 3b.

Fig. 4 compares the H_2S fluxes with and without the presence of metals. From the fact that the initial fluxes with and without the presence of metals are about equal, one may conclude that no chemical enhancement of H_2S absorption is observed at the applied conditions. This is due to the fact that the bulk concentrations of Cu^{2+} and Zn^{2+} are much lower than the concentration of H_2S at the liquid side of the interface, resulting in very low values of the infinite enhancement factor for penetration model is defined by ($E_{a,\infty}$) (Westerterp et al., 1987)

$$E_{a,\infty} = 1 + \frac{c_{\mathrm{Me}}^{\mathrm{bulk}}}{c_{\mathrm{H_2S}}^{i}} \left(\frac{D_{\mathrm{Me}}}{D_{\mathrm{H_2S}}} \right)^{0.5}. \tag{44}$$

Figs. 5a and b show the effects of initial pH and initial zinc concentration on the H_2S flux. A decrease in initial pH leads to somewhat lower H_2S fluxes even though the H_2S concentration at the initial pH of 5 is 10 times lower than at the initial pH of 3. A decrease in initial zinc concentration only has a small effect on the flux (Fig. 5b); apparently most H_2S initially is reacting with Cu^{2+} to form CuS, which is less soluble than ZnS.

Fig. 6 shows the effect of H_2S concentration on the decrease in copper and zinc concentrations with time in the bulk. Increasing the gas concentration will increase the rate of metal depletion in the solution. As to be expected the calculated flux for pure H_2S gas is around 10 times higher than in the case of 10 vol% H_2S. The flux slightly decreases with time due to the decrease in metal concentration and the decrease in pH that tends to push the equilibrium towards H_2S rather than S^{2-}, resulting in a lower driving force for mass transfer and lower precipitation rates. From the differences between the disappearance rates of Zn^{2+} and Cu^{2+} one

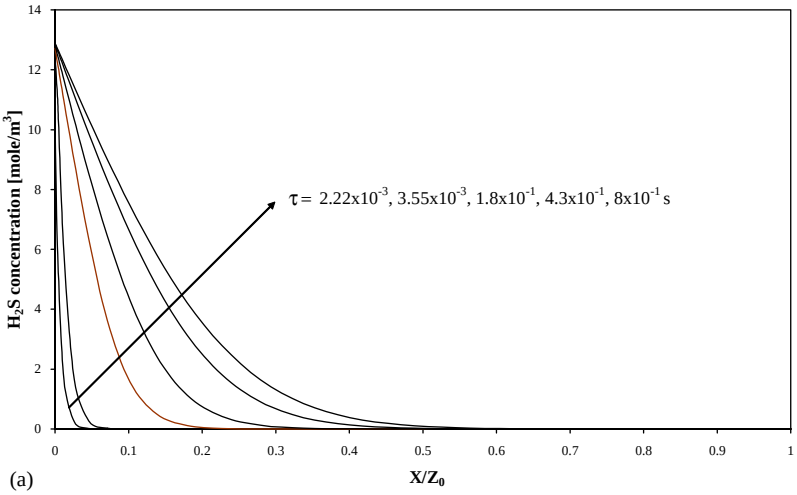

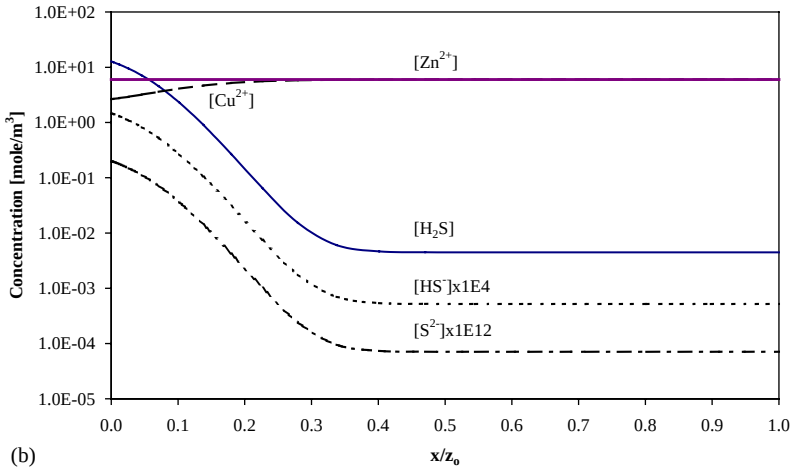

Fig. 3. (a) Concentrations profiles for H_2S gas (mol/m^3) in the liquid package during the penetration time. Conditions: $[H_2S] = 10$ vol%, $[Cu^{2+}]_{initial} = 6$ mol/m^3, $[Zn^{2+}]_{initial} = 6$ mol/m^3, initial pH = 5, volume of liquid = 1 l, $a = 0.785$ m^2/m^3, $k_{m,L} = 5 \times 10^{-5}$ m/s, $k_{m,g} = 1 \times 10^{-2}$ m/s, $T = 298$ K, $P = 1$ bar. (b) Typical concentrations profile for H_2S, HS^-, S^{2-}, Me_1^{2+} and Me_2^{2+} (mol/m^3) in the liquid package after the penetration time. Conditions: $[H_2S] = 10$ vol%, $[Cu^{2+}]_{initial} = 6$ mol/m^3, $[Zn^{2+}]_{initial} = 6$ mol/m^3, initial pH = 5, volume of liquid = 1 l, $a = 0.785$ m^2/m^3, $k_{m,L} = 5 \times 10^{-5}$ m/s, $k_{m,g} = 1 \times 10^{-2}$ m/s, $T = 298$ K, $P = 1$ bar.

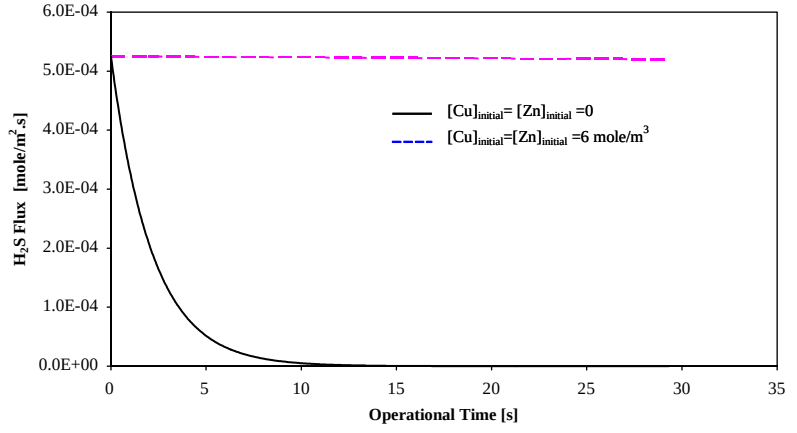

Fig. 4. Effect of the presence of precipitating metal ions on the flux of H_2S. Conditions: $[H_2S] = 10$ vol%, $[Cu^{2+}]_{initial} = 6$ mol/m^3, $[Zn^{2+}]_{initial} = 6$ mol/m^3, initial pH = 5, volume of liquid = 1 l, $a = 0.785$ m^2/m^3, $k_{m,L} = 5 \times 10^{-5}$ m/s, $k_{m,g} = 1 \times 10^{-2}$ m/s, $T = 298$ K, $P = 1$ bar.

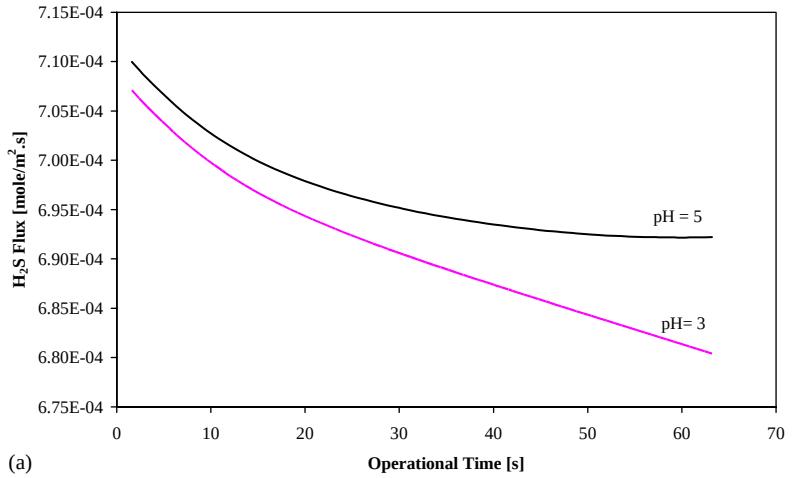

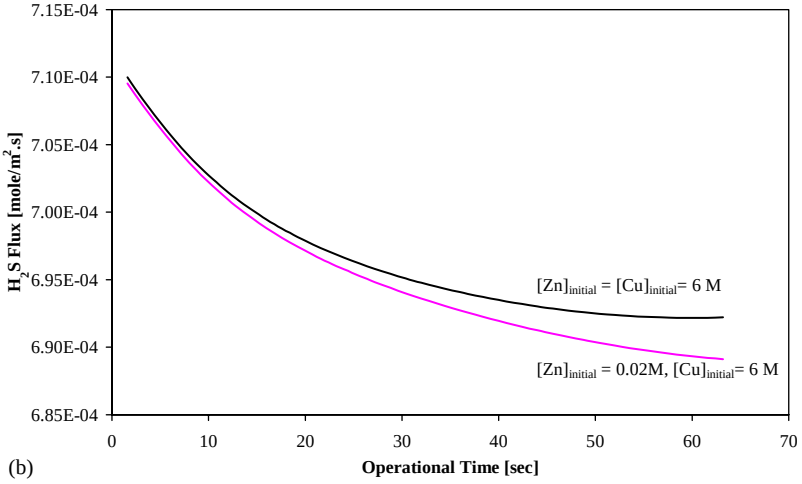

Fig. 5. (a) Effect of initial pH on the H_2S flux. Conditions: $[H_2S] = 10$ vol% for $pH_{initial} = 5$, $[H_2S] = 100$ vol% for $pH_{initial} = 3$, $[Cu^{2+}]_{initial} = 6$ mol/m^3, $[Zn^{2+}]_{initial} = 6$ mol/m^3, volume of liquid = 1 l, $a = 0.785$ m^2/m^3, $k_{m,L} = 7.2 \times 10^{-5}$ m/s, $k_{m,g} = 1 \times 10^{-2}$ m/s (only with $pH_{initial} = 5$), $T = 298$ K, $P = 1$ bar. (b) Effect of Zn^{2+} initial concentration on the H_2S flux. Conditions: $[H_2S] = 10$ vol%, $[Cu^{2+}]_{initial} = 6$ mol/m^3, initial pH = 5, volume of liquid = 1 l, $a = 0.785$ m^2/m^3, $k_{m,L} = 7.2 \times 10^{-5}$ m/s, $k_{m,g} = 1 \times 10^{-2}$ m/s, $T = 298$ K, $P = 1$ bar.

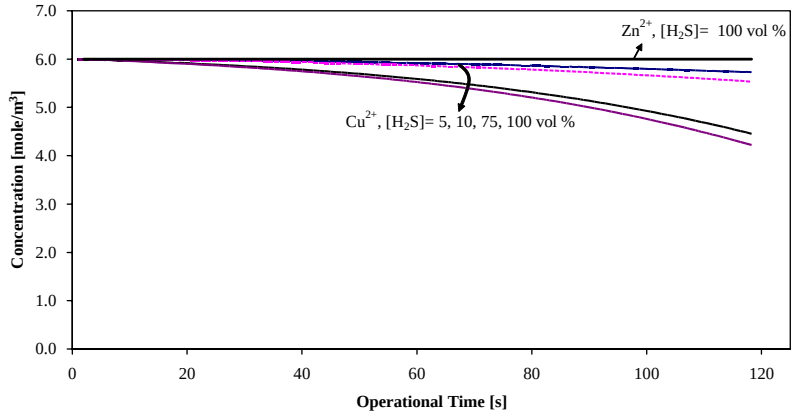

Fig. 6. Effect of H_2S concentration on the concentrations of Cu^{2+} and Zn^{2+} in the liquid bulk. Conditions: $[Cu^{2+}]_{initial} = 6$ mol/m^3 (lower 4 lines), $[Zn^{2+}]_{initial} = 6$ mol/m^3 (upper line), initial pH = 5, volume of liquid = 1 l, $a = 0.785$ m^2/m^3, $k_{m,L} = 5 \times 10^{-5}$ m/s, $k_{m,g} = 1 \times 10^{-2}$ m/s (in case of gas mixtures), $T = 298$ K, $P = 1$ bar.

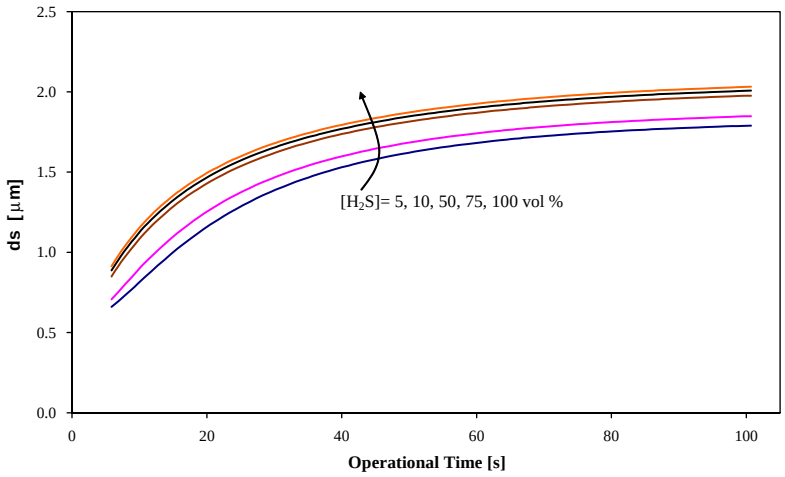

Fig. 7. Effect of H_2S concentration on average particle size of CuS precipitation in the reactor. Conditions: $[Cu^{2+}]_{initial}$=6 mol/m^3, $[Zn^{2+}]_{initial}$=6 mol/m^3, initial pH = 5, volume of liquid = 1 l, $a = 0.785$ m^2/m^3, $k_{m,L} = 5 \times 10^{-5}$ m/s, $k_{m,g} = 1 \times 10^{-2}$ m/s (in case of gas mixtures), $T = 298$ K, $P = 1$ bar.

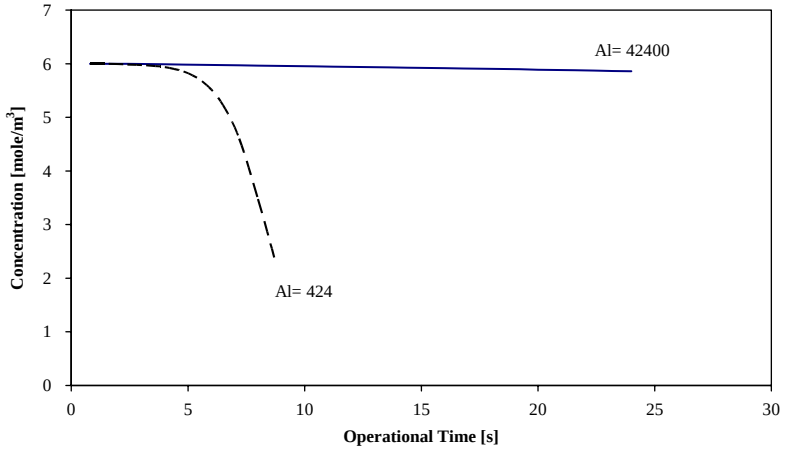

Fig. 8. Effect of Hinterland ratio on Cu^{2+} concentration depletion in the liquid bulk. Conditions: $[H_2S]$ = 10 vol%, $[Cu^{2+}]_{initial}$ = 6 mol/m^3, $[Zn^{2+}]_{initial}$ = 6 mol/m^3, initial pH = 5, volume of liquid = 1 l, $k_{m,L} = 5 \times 10^{-5}$ m/s, $k_{m,g} = 1 \times 10^{-2}$ m/s, $T = 298$ K, $P = 1$ bar.

may again conclude that CuS precipitates faster than ZnS, illustrating the possibilities for selective metal removal.

The effect of H_2S concentration on the Sauter diameter (d_s) of the CuS precipitate is shown in Fig. 7. Increasing the H_2S concentration in the gas phase apparently leads to an increase in average diameter: the H_2S flux increases while the concentration of S^{2-} remains almost constant due to the fast precipitation reactions (around the equilibrium concentration) which leads to an increase of metal depletion, a decrease in supersaturation and consequently lower nucleation rates and bigger diameters of the fewer particles.

The effects of the Hinterland ratio $[Al = k_L/(aD)]$ on copper depletion and average particle diameter are demonstrated in Figs. 8 and 9. A decrease in Hinterland ratio (or an increase in specific gas–liquid surface area) leads to faster Cu depletion as precipitation is fully controlled by the rate of mass transfer. On the other hand, the formed particles become smaller because of higher average supersaturation values and consequently higher nucleation rates. So, increasing the contact area will accelerate the removal rate of the metal ions but at the same time yield smaller particles as more particles are formed and crystal growth is less.

The effect of the mass transfer coefficient on copper depletion and average particle diameter is shown in Figs. 10 and 11. As to be expected increasing $k_{m,L}$ values yield higher rates of precipitation. On the other hand, the average particle diameter obtained after longer operation times is increasing at decreasing $k_{m,L}$ values (Fig. 11). A decreasing $k_{m,L}$ value corresponds to a higher contact time τ and hence lower

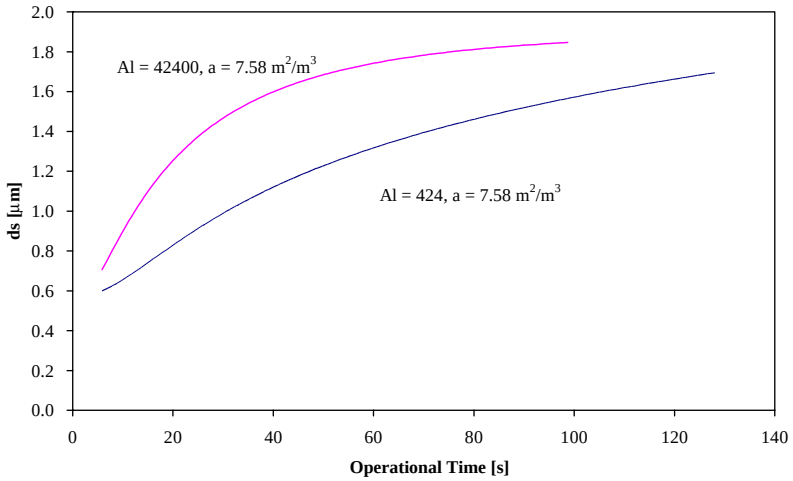

Fig. 9. Effect of Hinterland ratio on the average surface diameter of CuS precipitate in reactor. Conditions: $[H_2S] = 10$ vol%, $[Cu^{2+}]_{initial} = 6$ mol/m^3, $[Zn^{2+}]_{initial} = 6$ mol/m^3, initial pH = 5, volume of liquid = 1 l, $k_{m,L} = 5 \times 10^{-5}$ m/s, $k_{m,g} = 1 \times 10^{-2}$ m/s, $T = 298$ K, $P = 1$ bar.

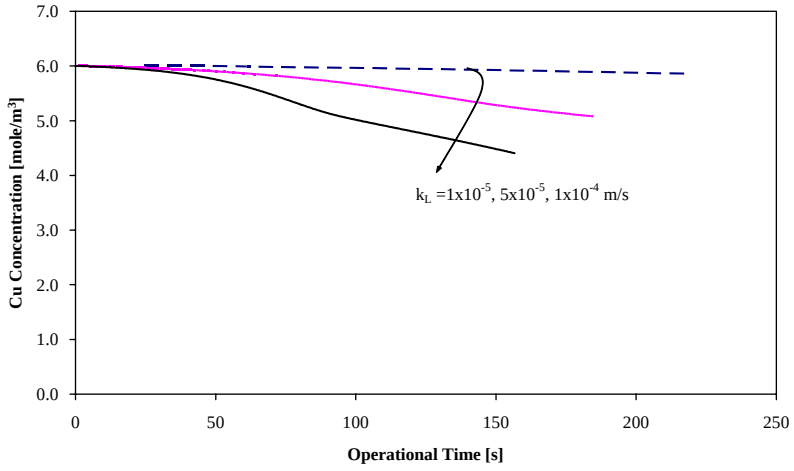

Fig. 10. Effect of mass transfer coefficient on Cu^{2+} depletion in the liquid bulk. Conditions: $[H_2S] = 10$ vol%, $[Cu^{2+}]_{initial} = 6$ mol/m^3, $[Zn^{2+}]_{initial} = 6$ mol/m^3, initial pH = 5, volume of liquid = 1 l, $a = 0.785$ m^2/m^3, $k_{m,g} = 1 \times 10^{-2}$ m/s, $T = 298$ K, $P = 1$ bar.

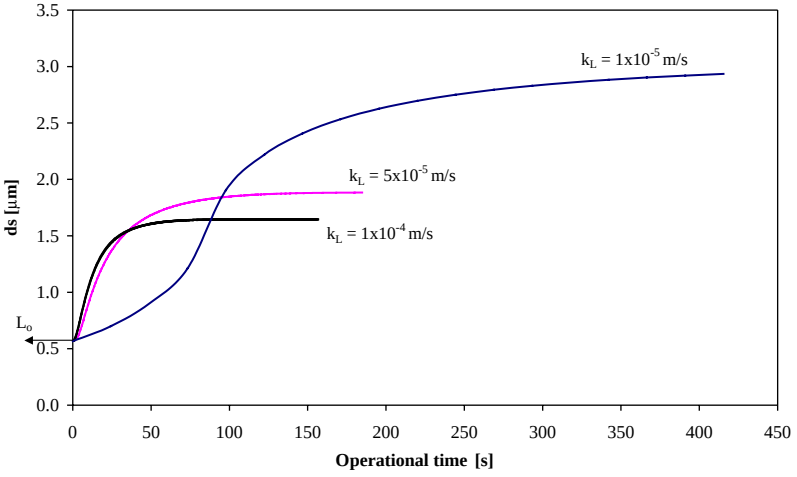

Fig. 11. Effect of mass transfer coefficient on the Sauter diameter of CuS precipitate in reactor. Conditions: $[H_2S] = 10$ vol%, $[Cu^{2+}]_{initial} = 6$ mol/m^3, $[Zn^{2+}]_{initial} = 6$ mol/m^3, initial pH = 5, volume of liquid = 1 l, $a = 0.785$ m^2/m^3, $k_{m,g} = 1 \times 10^{-2}$ m/s, $T = 298$ K, $P = 1$ bar.

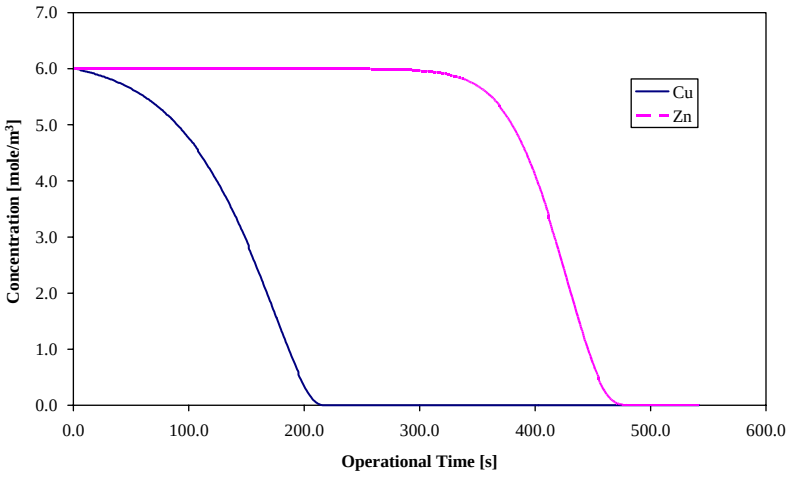

Fig. 12. Concentration of Cu^{2+} and Zn^{2+} in the bulk liquid as a function of operation time. Conditions: $[H_2S] = 10$ vol%, $[Cu^{2+}]_{initial} = 6$ mol/m^3, $[Zn^{2+}]_{initial} = 6$ mol/m^3, initial pH = 5, volume of liquid = 1 l, $a = 0.785$ m^2/m^3, $k_{m,L} = 5 \times 10^{-5}$ m/s, $k_{m,g} = 1 \times 10^{-2}$ m/s, $T = 298$ K, $P = 1$ bar.

average supersaturation values due to depletion of the metal ions present in the package. Lower supersaturation values are favourable for crystal growth as growth is less sensitive to supersaturation than nucleation (compare value of $n = 3$ in Eq. (26) with $g = 1.3$ in Eq. (25)). This result is in agreement with the findings of Wachi and Jones (1991). At shorter operational times things may seem a bit confusing. At lower $k_{m,L}$ values it takes more time for the crystals to enter the bulk. The first calculation results are therefore delivered after longer operation times.

Finally, the model predicts selective precipitation of Copper as shown by Fig. 12. The difference in the solubilities of CuS and ZnS obviously is so large that all S^{2-} initially reacts with Cu^{2+}. Only after all Cu^{2+} has been consumed Zn^{2+} starts to precipitate.

5. Conclusions

A mathematical model has been developed to simulate the simultaneous precipitation of two heavy metal ions with H_2S gas. The model predicts higher precipitation rates for higher pH values and higher H_2S concentrations. Furthermore, selective precipitation of the least soluble metal can be observed in cases where the solubilities of the two metal sulphides differ much. The rate of precipitation is fully controlled by mass transfer of the H_2S, higher H_2S concentrations and higher specific surface areas, therefore yielding higher precipitation rates. Chemical enhancement of H_2S transfer has not been found at the realistic metal concentrations applied on the model. The size of the obtained crystals is predicted to increase with H_2S concentration, but to decrease with specific surface area and liquid side massk transfer rates. These results illustrate the importance of reactor layout and operating conditionson the process gas–liquid precipitation.

Notation

a	specific surface area, m^2/m^3
Al	Hinterkland ratio, dimensionless
B'	mass nucleation rate, mol/m^3 s
c_i^*	equilibrium concentration of species (i), mol/m^3
c_i^{bulk}	concentration of species (i) in the liquid bulk, mol/m^3
c_i	concentration of species (i) in the package, mol/m^3
[Cu]	concentration of copper ions, mol/m^3
d_s	Sauter diameter, m
D_i	diffusion coefficient of species (i), m^2/s
$E_{a,\infty}$	infinite enhancement factor, dimensionless
F	Faraday constant, C/mol
(g)	gas (subscript)
g	exponent of growth rate, dimensionless
G	linear growth rate, m/s
G'	mass growth rate, mol/m^3 s
H	height of the liquid in the reactor, m
$[H_2S]$	H_2S concentration, mol/m^3
i	interfacial subscript
k	reaction rate constant, SI unit
k_b	constant in Eq. (24), 1.38×10^{-21}
k_{eq}	equilibrium constant, SI unit
k_g	growth rate constant, m/s
$k_{m,g}$	gas side mass transfer coefficient, m/s
$k_{m,L}$	liquid side mass transfer coefficient, m/s
k_n	nucleation rate constant, #/m^4 s
k_{sp}	solubility product constant, mol^2/m^6
k_w	ionic product of water mol^2/m^6
(l)	liquid (subscript)
L_0	critical nucleus diameter, m
L	particle diameter, m

J_n	rate of nucleation, #/m^4 s
m	distribution coefficient, dimensionless
n	exponent of nucleation, dimensionless
n_i	particle size density of species (i), #/m^3 m
p	particle
r	radius of particle
r_i	rate of consumption of species (i), mol/m^3 s
R	universal gas constant, Pa m^3/mol K
t	Time, s
T	temperature, K
x	Distance (depth of the package), m
z	ionic valency, dimensionless
z_0	package thickness, m
[Zn]	zinc ions concentration, mol/m^3

Greek letters

α	volume to length shape factor, dimensionless
β	surface to length shape factor, dimensionless
η	viscosity of the solution, Pa m/s
ρ	crystal density, mol/m^3
τ	contact time, s
ϕ	electrostatic potential gradient, V/m

Acknowledgements

This project was supported with a grant of the Dutch Program EET (Economy, Ecology, Technology) a joint initiative of the Ministries of Economic Affairs, Education, Culture and Sciences, and of Housing, Spatial Planning and Environment. This program is coordinated by the EET Program Office, a partnership of Senter and Novem. Hans Kuipers and Martin Van Sint Annaland are acknowledeged for their help in the mathematical field.

References

Al-Rahed, M.H., Jones, A.G., 1999. CFD modeling of gas–liquid reactive recipitation. Chemical Engineering Science 54, 4779–4784.

Baker, G.A., Oliphant, T.A., 1960. An implicit, numerical method for solving the two-dimensional heat equation. Quarterly of Applied Mathematics 17, 361–373.

Higbie, R., 1935. The rate of absorption of pure gas into a still liquid during short periods of exposure. Transactions of A.I.Ch.E. 31, 365.

Hostomsky, J., Jones, A., 1995. Penetration model of gas–liquid reactive precipitation of calcium carbonate crystals. Transactions of I.Ch.E.M.E. 73(A), 241–245.

Jones, A.G., Hostomsky, J., Zhou L., 1992. On the effect of liquid mixing rate on primary crystal size during the gas–liquid precipitation of calcium carbonate. Chemical Engineering Science 47(13/14), 3817–3824.

Mersmann, A., 1995. Crystallization Technology Handbook. Marcell Dekker, New York, Basel.

Narayan, S.T., 1991. Batch crystallizers. Reviews in Chemical Engineering 7 (3–4), 213–352.

Newman, J.S., 1973. Electrochemical Systems. Prentice-Hall Inc., Englewood Cliffs, NJ.

Paques, www.paques.nl.

Randolph, A.D., Larson, M.A., 1988. Theory of Particulate Processes, 2nd Edition. Academic Press, New York.

Sutherland, W.A., 1905. Dynamical theory of diffusion for non-electrolytes and the molecular mass of albumin. Philosophical Magazine 9, 781–785.

Versteeg, G.F., Kuipers, J.A.M., Beckum, F.P.H., Van Swaaij, W.P.M., 1989. Mass transfer with complex reversible chemical reactions—I. Single Reversible Chemical Reaction. Chemical Engineering Science 44 (10), 2295–2310.

Wachi, S., Jones, A., 1991. Mass transfer with chemical reaction and precipitation. Chemical Engineering Sciences 46 (4), 1027–1033.

Wachi, S., Jones, A., 1992. Dynamic modeling of particle size distribution and degree of agglomeration during precipitation. Chemical Engineering Sciences 47 (12), 3145–3148.

Wachi, S., Jones, A., 1995. Aspect of gas–liquid reaction systems with precipitate particle formation. Reviews in Chemical Engineering 11 (11), 1–51.

Westerterp, K.R., Swaaij, W.P.M., Beenackers, A.A.C.M., 1987. Chemical Reactor Design and Operation. Wiley, New York.